

This document is the Accepted Manuscript version of a Published Work that appeared in final form in **ACS Applied Nano Materials**, copyright © American Chemical Society after peer review and technical editing by the publisher. To access the final edited and published work see [<https://pubs.acs.org/doi/full/10.1021/acsanm.8b00301>].

Mesoporous SiC with Potential Catalytic Application by Electrochemical Dissolution of Polycrystalline 3C-SiC

Svitlana Gryn^{a,b}, Tetyana Nychyporuk^c, Igor Bezverkhy^d, Dmytro Korytko^{a,b}, Viacheslav Iablokov^e, Vladimir Lysenko^c, Sergei Alekseev^{a,b}

^a Taras Shevchenko National University of Kyiv, 64, Volodymyrska St., 01601 Kyiv, Ukraine

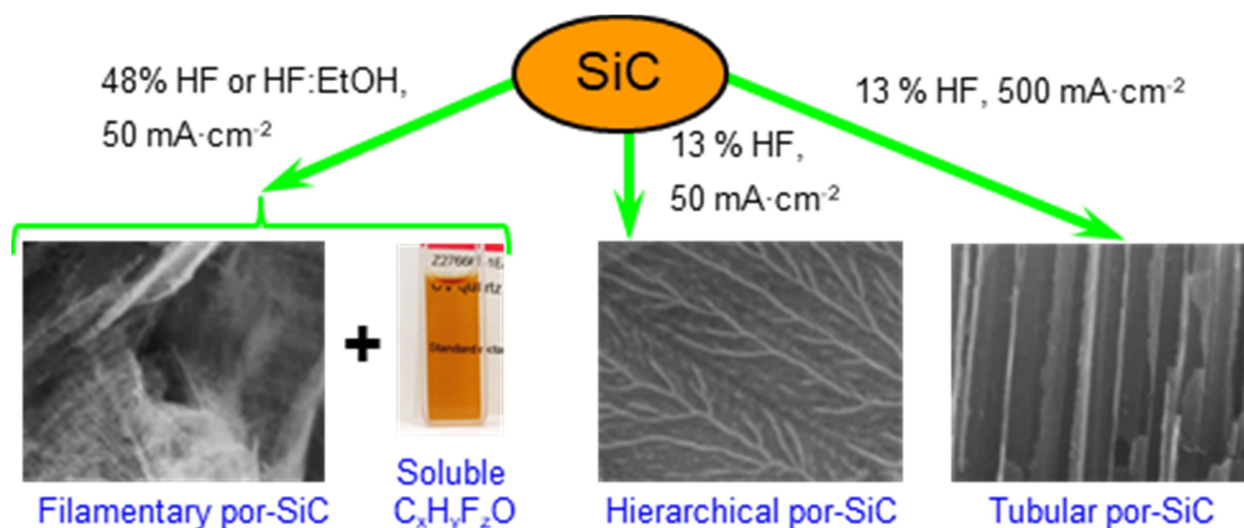
^b Science Park Kyiv Taras Shevchenko University, 60, Volodymyrska St., 01033 Kyiv, Ukraine

^c University of Lyon, Nanotechnology Institute of Lyon (INL), UMR CNRS 5270, INSA de Lyon, France

^d Laboratoire Interdisciplinaire Carnot de Bourgogne, UMR CNRS 6303, Université de Bourgogne, France

^e Voiland School of Chemical Engineering and Bioengineering, Washington State University, Pullman, Washington 99164, USA.

TOC Figure



Abstract

Electrochemical dissolution of highly-doped ($\rho \sim 1 \text{ m}\Omega\cdot\text{cm}$, n-type) polycrystalline 3C-SiC in HF/H₂O and HF/H₂O/ethanol solutions allowed to produce porous silicon carbide (por-SiC), and soluble carbon fluorooxide nanoparticles as a by-product. The por-SiC is a well-crystalline material with large pore volume, surface area close to $100 \text{ m}^2 \text{ g}^{-1}$ and open mesoporous structure. The surface of por-SiC is covered with a thin carbon-enriched layer, bearing carboxylic acid groups. Depending on the SiC resistivity, etchant composition and current density, three different types of por-SiC morphology, namely a macroporous tubular, mesoporous hierarchical and mesoporous filamentary were revealed. A qualitative physical model of SiC electrochemical dissolution, based on the phenomena of quantum confinement, charge carriers trapping onto the surface defects, and the surface passivation, was proposed, and successfully interpreted the dependencies of por-SiC morphology and material balance on the etching conditions. The por-SiC is anticipated to be a prospective material for catalytic, nanofiltration and sensing applications.

1. Introduction

Silicon carbide demonstrates the properties of a wide band-gap semiconductor ($\Delta E = 2.36$ eV for 3C-SiC polytype) combined with high thermal conductivity ($120 \text{ W m}^{-1} \text{ K}^{-1}$ for 3C-SiC as compared to $1.4 \text{ W m}^{-1} \text{ K}^{-1}$ for SiO_2), and outstanding thermal, mechanical and chemical stability¹. These unique features make the SiC-based nanostructures (porous SiC (por-SiC) and SiC nanowires (SiC NWs)) promising for the application as catalysts supports²⁻⁵, photocatalysts⁶⁻⁸, biosensors⁹, supercapacitors^{10,11}, production of porous carbide-derived carbons¹², nanoporous membranes¹³ as well as for further grinding to produce SiC nanoparticles¹⁴⁻¹⁷.

As the other nanostructures, the por-SiC can be obtained by a “bottom-up” approach, which includes the formation of the por-SiC structure from low-molecular substances, as well as a “top-down” approach, through porosification of bulk SiC¹⁸. Reactions used for the “bottom-up” synthesis of the por-SiC include carbothermal^{19,20} or magnesiothermal^{21,22} reduction of C/SiO₂ nanocomposites, interaction of porous carbon with silicon monoxide^{23,24} or silicon powder^{11,25,26}. Significant attention was paid to a nanocasting method based on the thermal decomposition of special preceramic polymer (polycarbosilane) confined inside the pores of solid SiO₂ template²⁷⁻³¹, assembled around semifluorinated alkane molecular template³² or included as a polycarbosilane unit into the block copolymer^{33,34}. However, the por-SiC obtained by carbothermal reduction or by reaction with SiO commonly demonstrates low surface area, disordered porous morphology, and wide pore size distribution due to the vapor-phase reaction mechanisms³⁵. The nanocasting-derived por-SiC with well-defined morphology is rather semi-amorphous than crystalline material. All the other “bottom-up” nano-SiC materials possess a lot of crystalline structure imperfections.

Thermal conductivity³⁶, chemical stability³⁷, optical, and electrical properties of the SiC are determined substantially by the degree of its crystalline structure ordering. This fact may cause essential limitations of the “bottom-up” nano-SiC applicability in different fields. On the other hand, the “top-down” nano-SiC prepared by partial dissolution of the bulk SiC is considered to

contain a minimal amount of crystallite imperfections, due to their low content in the initial bulk SiC, and due to their lower chemical stability as compared to perfect crystallites. Application of the electric current as an oxidant makes etching process well-controllable and reproducible.

Generally, the first claims of electrochemical etching of the SiC were electropolishing and patterning of its surface; different electrolytes, such as NaOH, KOH, H₂O₂, HCl, H₂SO₄, and HF were used for this purpose [see review ³⁸ and references therein]. The HF (in combination with H₂O and/or organic solvents) was found to be the most efficient among them due to its activity in the dissolution of surface-present SiO₂. The formation of por-SiC layers under SiC anodization was frequently considered as undesirable side process until in early 1990-th, in pursuit of Canham's famous publication on photoluminescence of porous silicon³⁹, several research groups⁴⁰⁻⁴³ described intense photoluminescence of the por-SiC.

The morphology of the pores of electrochemically-derived por-SiC is determined by a wide set of process parameters, particularly by electrolyte composition, current density, SiC substrate polytype (more than 200 polytypes are known⁴⁴), SiC doping level and type. Other factors include the presence of defects, such as vacancies and micropipes, intensity and wavelength of illumination. The latter is crucial for medium or low conductivity n-type SiC, highly-resistant to electrochemical etching in the dark due to the lack of holes near the surface.

Furthermore, different from the silicon, the SiC is a polar semiconductor. As a result, the polar planes of SiC structure, such as Si plane ((0001) in hexagonal polytypes, (111) in cubic polytype) and C plane ((000 $\bar{1}$) and ($\bar{1}\bar{1}\bar{1}$), correspondingly), possess significantly different chemical properties. According to refs. ^{45,46}, the geometry of mesopores in n-type por-4H-SiC originates mainly from the highest chemical stability of "Si-planes" ((0001) and (1 $\bar{1}$ 0 $\bar{2}$) for 4H SiC polytype) towards oxidation. The pore propagation preferably occurs normal to (11 $\bar{2}$ 0) planes of 4H-SiC, which atomic structures correspond to one of the (110) plane of 3C-SiC. All aforementioned makes the morphologies of the por-SiC much more variable and less-predictable, than those reported for porous silicon.

The pore morphology was characterized mainly for the por-SiC derived from monocrystalline n-type 4H-SiC and 6H-SiC wafers⁴⁷. Three types of mesoporous morphologies exhibiting “chevron-like”, “triangular” and “dendritic” pore cross-sections and characteristic pore sizes in the range of 10 – 50 nm are commonly reported. Two macroporous morphologies, such as “sinuous” with 100 – 300 nm pores with partially rafted walls and “columnar” with 200 – 300 nm linear channels are also acknowledged.

An influence of the etching conditions on the pore morphology has a complex nature due to the non-uniform doping of the SiC as well as the necessity of illumination for n-type SiC wafers. Therefore, different morphologies coexist within the same layer at different depth and even laterally. Particularly, next general points have been summarized from the literature data:

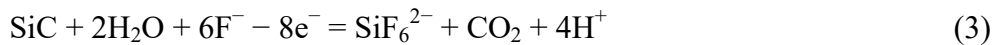
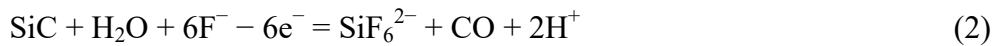
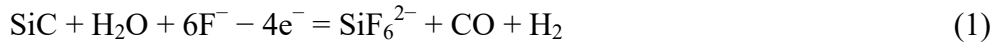
- i) Increase of the current density (j) led to a consecutive morphology evolution in the next order: “chevron-like” - “triangular” - “dendritic” - “sinuous” - “columnar”^{46,48}. The order of mesoporous morphology evolution from the “chevron” to “dendritic” in the depth of the porous layer is also usually kept⁴⁹⁻⁵¹.
- ii) Within the same morphology, an increase of the j resulted in the increase of the porosity and corresponding narrowing of the pore walls and growing of the pore size⁵²⁻⁵⁴. However, the interpore distance remains constant; probably it is determined by the thickness of a space charge region (SCR) blocking the initiation of neighbor pores⁴⁶.
- iii) Increase of the samples' resistivity as well as decrease of illumination intensity for low-conducting n-type SiC resulted in porous layer inhomogeneity and appearance of the macropores⁴⁸⁻⁵⁵.
- iv) The morphology of por-SiC is very sensitive to the crystalline face exposed to the etching. Particularly, the “C-face” etches faster compared to the “Si-face”, however the resulted morphology is significantly less ordered^{46,50}.

The porosification of any SiC substrates, other than the hexagonal n-type wafers, is comparatively less studied due to their low accessibility. The p-type hexagonal por-SiC

demonstrates “branched” and “filamentary” mesoporous morphologies, less ordered than those of n-type por-SiC⁵². Porous 3C-SiC⁴⁷, derived from monocrystalline wafers, demonstrates triangular and “fish-bone” morphologies (vertical pore trunks with short and nearly horizontal mesopores), similar to ones found recently for por-Ge⁵⁶. The triangular pores of por-3C-SiC form rows along the (111) direction, and, possibly, propagate along the (100) and/or (110) directions.

The electrolyte composition is the least studied parameter in the por-SiC preparation. Commonly, the electrolytes containing 5-25 wt% of HF and up to 50% of ethanol are used. According to refs.^{51,57}, the concentration of HF and additives (ethanol, acetic acid, surfactants, H₂O₂ and KCl) influences significantly on the por-SiC morphology; however, no general tendency was possible to reveal from the data provided. One fact seems unavoidable, that no por-SiC was formed in extremely diluted (< 0.2 wt%) HF solutions due to electropolishing process⁵².

The chemistry of SiC electrochemical porosification also appeared complicated. The number of electrons (γ) generated under dissolution of a single SiC “molecule” is varied in the range from 5 to 7 depending on the anodization conditions^{52,58}. Following concurrent reactions (1-3) were assumed due to this fact:



As the formation of hexafluorosilicate is doubtless, the transformations of carbon under SiC etching are not as simple as they seem to be. According to our recent work⁵⁹, the organic-like oligomeric compound readily soluble in polar solvents and named carbon fluorooxide (CFO) is formed. The sublayer of the chemisorbed CFO, remained after etching, is a possible origin of carbon enrichment of the por-SiC surface, described in numerous papers^{49,60,61}.

According to all aforementioned, electrochemical porosification is an efficient route to produce well-crystalline por-SiC with controllable parameters. Hitherto, its application is limited to the porous layers on semiconductor-grade wafers and production of the SiC nanoparticles.

Herein, we describe the porosification of monolithic low resistivity (n-type, $\sim 1 \text{ m}\Omega\cdot\text{cm}$) chemical vapor deposition (CVD) polycrystalline 3C-SiC substrates, readily available to prepare the por-SiC in gram quantities. High doping level of these substrates allowed us to avoid influence of such uncontrollable etching factor as illumination due to the possibility of holes tunneling through the narrow SCR.

The morphology of the por-SiC was studied mainly by SEM and N_2 -adsorption isotherms; additional characterization of the por-SiC structures and surface chemistry was performed by means of powder XRD, TEM, FTIR, and solid-state NMR. Analysis of the dependencies of por-SiC morphology and material balance (yields of por-SiC and CFO products) on the etching conditions allowed us to propose a qualitative physical model of the SiC electrochemical dissolution, based on the phenomena of quantum confinement and surface passivation. The conditions of etching were optimized to prepare highly crystalline por-SiC with open mesoporous morphology. This material is perfectly suitable as a support in highly exothermic reactions. Obtained por-SiC samples have been used to host cobalt nanoparticles demonstrating superior catalytic performance in highly exothermic Fischer-Tropsch reaction⁶². The catalytic results will be published in the forthcoming paper.

2. Experimental section

2.1. Porous SiC preparation by electrochemical etching

Monolithic CVD polycrystalline 3C-SiC plates ($\geq 99.9995\%$ SiC) with low resistivity were purchased from Rohm and Haas; the specification is available on a web-site of Dow Chemicals Company⁶³. The anodization was performed in the Teflon cells with copper electrodes as backside contacts and gold counter-electrodes. Three 4 mm thick, 100 mm diameter plates with the resistivities equal to 0.7; 1.6 and 4.0 $\text{m}\Omega\cdot\text{cm}$ (n-type) were chosen for anodization in 60 cm^2 cell to produce powder samples for N_2 -adsorption analysis; small pieces of 1 mm thick 0.7 $\text{m}\Omega\cdot\text{cm}$ plate were anodized in 0.2 cm^2 cell for cross-sectional SEM analysis. The electrolytes consisted of HF (1-48 wt%), H_2O and EtOH (0, 25 or 50 vol%). A range of current

densities 25 – 1000 mA cm⁻² was used; no additional stirring was applied. Normally, the SiC surface subjected to etching was rough as a result of the multiple usages of the plates (after consecutive porous layer removal).

After the etching, the porous layers formed on top of the SiC plate were rinsed with DI water, dried and collected by mechanical scratching leading to brownish powders. To separate the por-SiC and the CFO⁵⁹, the powders were rinsed with EtOH under centrifugation. As the SiC plates were used for several times, the residues of por-SiC were thoroughly removed from the plate under mechanical action and EtOH rinse steps. Processes of SiC plates etching, samples work-up and CFO/SiC separation are schematically represented on the Fig. 1.

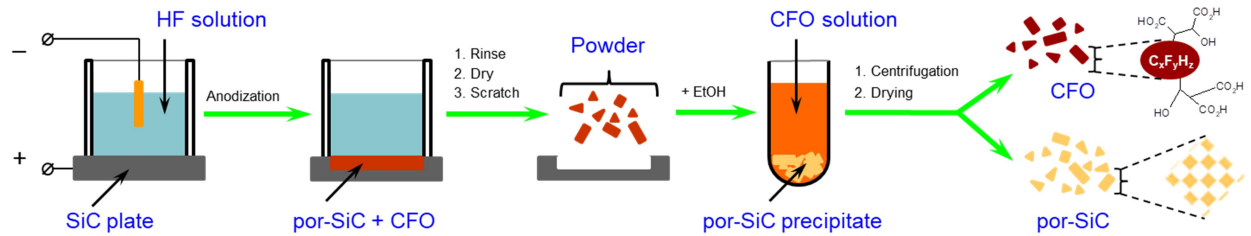


Fig. 1. Scheme of the samples preparation.

2.2. Characterization methods

To obtain the material balance parameters, the SiC plate, subjected to etching, was weighted on each stage of the process with ± 0.01 mg precision. The overall yield of the powder (Y) was calculated according to formula:

$$Y = \frac{m_1 - m_2}{m_0 - m_2} \cdot 100\%$$

where m_0 is the SiC plate mass before etching, m_1 is the plate mass after etching and drying, m_2 is the plate mass after complete powder removal. As the etching of the SiC plate provides a mixture of both, por-SiC and ethanol-soluble CFO⁵⁹, the por-SiC fraction in the powder (W(SiC), %) was determined as the ratio of dried powder masses after and before the ethanol rinsing.

Powder X-ray diffraction (XRD) patterns were collected on a Bruker Pan Analytical X'pert diffractometer equipped with CuK α X-ray source. FT-IR spectra were collected on a

Nicolet Nexus 470 spectrometer in pellets with KBr or in diffuse reflectance mode under ambient conditions. ^{29}Si MAS NMR spectrum (^1H cross-polarized) was recorded on Bruker Avance III 400 spectrometer at 79,495 MHz and 4.5 kHz rotation speed.

TEM images were taken on JEOL JEM 2100 high-resolution transmission electron microscope with an accelerating voltage 200 kV. Scanning electron microscope (SEM) images were taken using the ultra-high resolution Tescan MIRA 3 scanning electron microscope at an accelerating voltage of 10 kV. The nitrogen adsorption/desorption isotherm measurements were carried out using Micromeritics ASAP 2020 system at 77 K. Adsorption data were treated according to the BET method and BJH method with Harkins-Jura correction using a standard software of the instrument.

3. Results and discussion

3.1. Chemistry and material balance of the SiC etching

According to the literature data⁴⁰⁻⁵⁸, main variables, influencing the characteristics of electrochemically-derived por-SiC are the SiC plate resistivity (ρ), crystallographic orientation, composition of electrolyte, current density (j) and the action of light. SiC plates used in this study are polycrystalline as they were industrially obtained by CVD; hence, the influence of the crystallographic orientation was not possible to study. High conductivity ($\rho \sim 1 \text{ m}\Omega\cdot\text{cm}$) allowed etching of these n-type plates at reasonably low voltages without any additional illumination. Typically the voltage does not exceed 12 V between the two electrodes in the large cell (60 cm² area; 10 cm distance). Therefore, the etching process is probably governed only by electrochemical reactions, proceeding by the holes tunneling through the SCR. Breakdown processes taking place at high voltage during etching of low-doped n-type semiconductors in the dark could be excluded. As a result, an influence of illumination in the studied case should be less significant than for low-doped SiC wafers, and this parameter was not taken in account. Our preliminary data demonstrates, that the quantity of the electricity (Q) passed through the etched

area has no or little impact on the por-SiC morphology and yield. So, for each series of the samples the value of Q was kept constant.

Table 1. Etching conditions and material balance parameters of por-SiC powders

Sample	Electrolyte	j, mA·cm ⁻²	Y, %	W (SiC), %
Initial plate 0.7 mΩ·cm				
1	*HF:EtOH (1:1)	25	45	6
2		50	33	6
3		100	13	18
4		200	5	71
5	HF:EtOH (3:1)	50	38	16
6		100	37	25
7	HF (5%)	50	15	100
8	HF (13%)	25	19	100
9		50	20	100
10		100	14	100
11	HF (26%)	25	13	86
12		100	14	77
13	HF (48%)	25	24	19
14		50	45	15
15		100	6	6
Initial plate 1.6 mΩ·cm				
16	HF (13%)	50	39	100
17	HF:EtOH (1:1)	50	32	26
Initial plate 4.0 mΩ·cm				
18	HF (13%)	50	45	100
19	HF:EtOH (1:1)	50	32	52

* means HF(48%):EtOH 1:1 (v/v)

The quantity of the electricity (Q) is equal to 0.1 A·h·cm⁻² for all the samples.

Material balance parameters: Y is the powder yield; W(SiC) is the fraction of por-SiC in powder.

The sample referencing in the following text includes the plate resistivity, electrolyte composition and current density (for example SiC0.7_HF13_50 for sample 9).

Only the plate resistivity, the electrolyte composition, and the current density were considered as variable parameters of the etching. A series of samples was prepared in the 60 cm² cell to obtain sufficient amounts of porous SiC for the material balance and N₂ adsorption characterization (Table 1). To cover a wider set of etching conditions, small 0.2 cm² samples (sSiC) were prepared from thin 0.7 mΩ·cm SiC plate exclusively for SEM studies to reveal their porous morphology. Referencing of these samples in following text includes the electrolyte

composition and current density. For example, sSiC_HF:EtOH(1:1)_50 means the sample, prepared in HF(48%):EtOH mixture (1:1, v/v) at $50 \text{ mA}\cdot\text{cm}^{-2}$.

The por-SiC layers on top of the SiC plate could easily be seen as lightly-colored (from sand-like to brown) deposits on the black surface (Fig. 2).

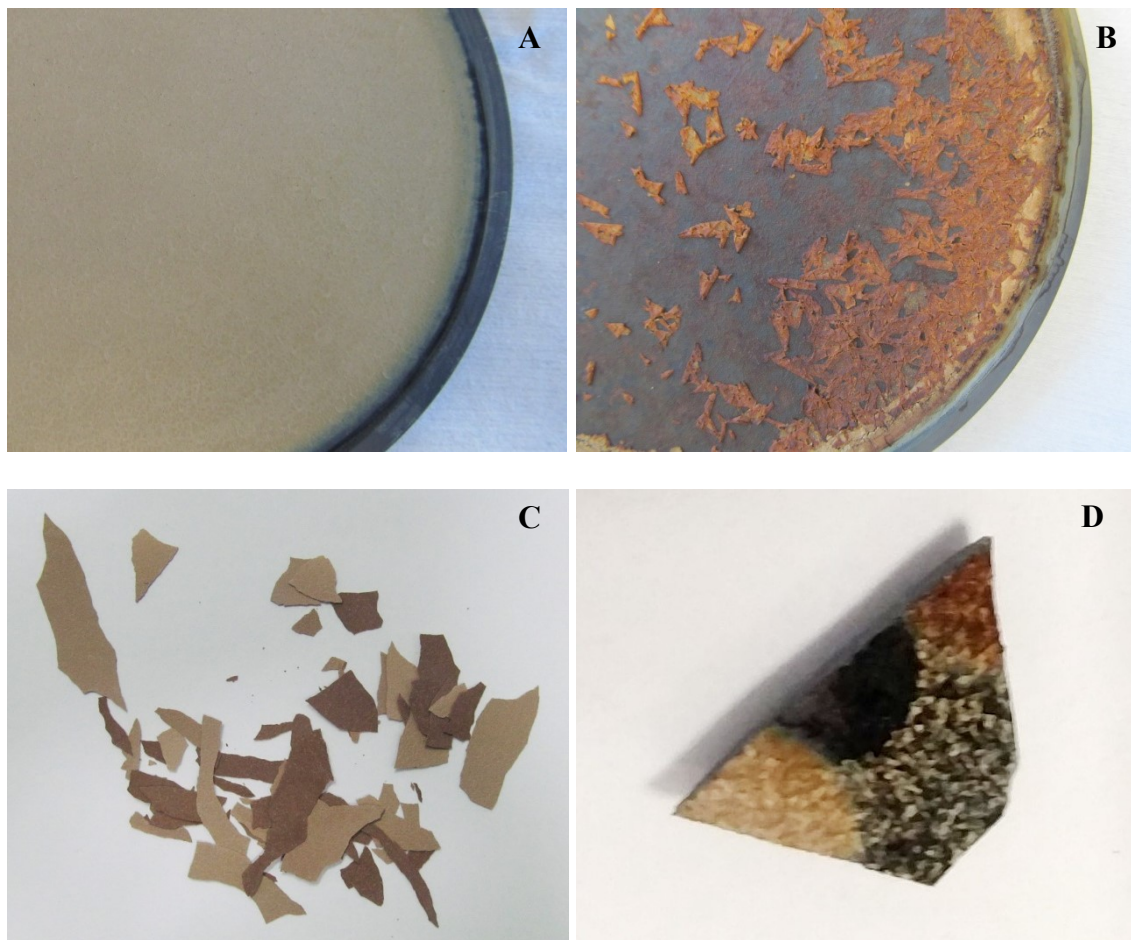


Fig. 2. Optical photos of porous SiC samples. Sample referencing corresponds to Tables 1 and 2. A) SiC0.7_HF13_50 before removal from the plate; B) SiC0.7_HF48_100; C) SiC4.0_HF13_50: brown - external surface, sand - internal surface; D) sSiC_HF1_50 (black), sSiC_HF2_50 (sand) and sSiC_HF48_50 (brown).

In some cases the porous layers detached completely (sSiC_HF1_50 and sSiC_HF:EtOH(1:1)_50) or partially (SiC0.7_HF48_100, sSiC_HF13_1000 and sSiC_HF48_50) from the plate during the stages of etching or rinsing. This phenomenon looks similar to well-known electropolishing of the silicon under anodization in HF solutions at high currents or low acid concentrations, when the electrochemical oxidation of Si is faster than the oxide dissolution in HF⁶⁴. This exactly happens for the samples sSiC_HF1_50 and sSiC_HF13_1000. However,

electropolishing at moderate currents in 48% HF or HF:EtOH (1:1) never takes place for the case of silicon (porous films produced in HF:EtOH (1:1) are stable in H₂O but are detached completely under EtOH rinse).

In general, the por-SiC layers studied herein could be completely and relatively easily removed from the plate under mechanical action and EtOH rinse. Obtained powders consisted of several- μm irregularly-shaped porous particles (Fig. S1, SI). The fraction of the powder, remaining in the solution after 5 min centrifugation at 2000 g, contained mainly flat-like particles with the size of tens to hundreds of nanometers. The samples prepared from 1.6 or 4 m $\Omega\cdot\text{cm}$ SiC plates in 13% HF showed the lowest porosity, and were not detachable by mechanical action. To peel them from the plates, either a strong current (0.5 A $\cdot\text{cm}^{-1}$, 10 min, 5 s etch + 20 s stop pulses) in 13% HF or continuous 15 min etching at 50 mA $\cdot\text{cm}^{-1}$ in HF:EtOH (1:1) were successfully applied. Thick (approx. 150 μm) mechanically strong por-SiC flakes were produced (see Fig. 2C). Sometimes, when higher resistivity SiC plates were etched in aqueous HF, porous SiC layers peeled off the plate spontaneously giving the SiC flakes similar to those shown in Fig. 2C. Probably, this observation is caused by the mechanical action of gas bubbles, formed due to the anodization and being trapped under the thick por-SiC layers with narrow pores.

Continuous etching of the SiC in either HF:H₂O or HF:EtOH mixtures resulted in yellow or brown colouration and foaming of the electrolyte (Fig. S2, SI). According to our recent work⁵⁹, this coloration takes place due to formation of the organic-like oligomeric compound named carbon fluoro-oxide (CFO). Actually, any porous deposits formed on the SiC surface after the anodization in HF solution should be considered as SiC/CFO mixture rather than a porous SiC. The properties of the CFO significantly depend on the electrolyte composition. The CFO formed in the HF:EtOH mixture is poorly soluble in H₂O, while the CFO formed in the aqueous HF dissolves in water rapidly (samples 11-15 in Table 1 were rinsed only by the electrolyte before drying to avoid their washout). This difference is probably governed by the esterification degree of the CFO carboxylic groups. However, the CFO of any type, studied in the present

work, demonstrates high solubility in ethanol allowing the efficient separation of the CFO from the por-SiC. The SiC/CFO ratio in the sample strongly affects its color (for instance, compare Fig. 2A and B), as the por-SiC after the EtOH rinse has a sand color and the CFO is brown or red-brown (Fig. S1, SI).

The powder yield (Y) and the fraction of porous SiC in the powder ($W(\text{SiC})$) were considered as material balance parameters (Table 1); the overall yield of porous SiC could be calculated as their product. Among the parameters of the etching process (ρ , j and electrolyte), the composition of an etchant and the plate resistivity seem to have the strongest and unambiguous impact on the material balance (Table 1, Fig. 3).

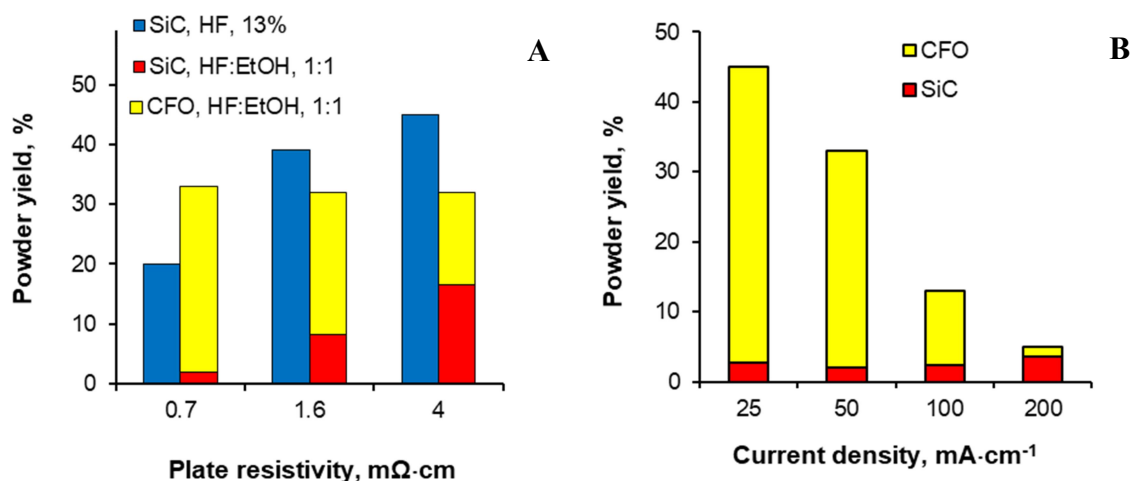


Fig. 3. A) Dependence of the overall powder yield of por-SiC prepared at $j = 50 \text{ mA}\cdot\text{cm}^{-2}$ on the plate resistivity; B) Influence of the current density on the SiC and CFO yields for samples prepared in HF:EtOH etchant from $0.7 \text{ m}\Omega\cdot\text{cm}$ SiC plate.

Etching of SiC either in highly concentrated HF or in HF:EtOH mixtures resulted in the high powder yields. However, the obtained powders were mainly composed of the CFO with a low fraction of por-SiC. Conversely, no soluble CFO fraction was found in the samples, formed in the diluted aqueous HF, probably due to high solubility of formed CFO in this electrolyte.

Growth of the plate resistivity from 0.7 to $4 \text{ m}\Omega\cdot\text{cm}$ resulted in significant increase in the powder yield and the fraction of SiC in the CFO-containing mixtures (if they were formed) associated with a noticeable decrease in the porosity. It can be easily seen by the change of

mechanical properties of the sample (SiC_0.7_HF13_50 – easily removable porous layer, while SiC1.6_HF13_50 and SiC4.0_HF13_50 – mechanically strong porous flakes, which should be intentionally peeled from the plate, see above).

Influence of the current density (j) showed entirely different behavior for ethanolic and aqueous HF etchants. For the HF:EtOH mixture growth of j resulted in a diminution of the powder yield accompanied by the growth of SiC fraction in it (Fig. 3B). Possibly, this dependence is caused by the growth of the CFO solubility in HF:EtOH with the j increase observed qualitatively by the etchant color darkening. For the aqueous 13% HF only a minor decrease in the powder yield with an increase in the current density was found for the range, presented in Table 1.

Another material balance parameter frequently reported in the literature^{52,58} is the number of electrons (γ) generated during the dissolution of a single SiC “molecule”. For the samples in Table 1 this parameter was found to be in the range of 6.1 to 7.2, showing some decrease with growth of j , $C(\text{HF})$, presence of ethanol in the electrolyte and SiC plate conductivity. However, possible presence of chemisorbed CFO in porous SiC, partial losses of the SiC powder during the etch as well as other factors giving significant data dispersion within the above range make this conclusion largely speculative.

Physicochemical properties of por-SiC samples, such as their crystalline structure, thermal stability, and chemical composition, appeared to be rather independent on the etching conditions. Their systematic characterization applying powder XRD, FTIR, ²⁹Si MAS NMR and TEM methods was performed on the example of por-SiC prepared from 0.7 mΩ·cm plate by 2 h etching in 13% aqueous HF at 50 mA cm⁻² (Sample 9, Table 1). Separation of the dried porous layer (Fig. 2A) provided approximately 0.3 g of sand color powder having a specific surface area of 118 m² g⁻¹, 0.67 cm³ g⁻¹ pore volume, and average pore size of about 23 nm.

Powder X-ray diffraction (XRD) pattern of the por-SiC (Fig. 4A) demonstrates intense peaks at 35.55, 59.92 and 71.69 2θ corresponding to (111), (220) and (311) planes of 3C-SiC,

respectively (Joint Committee on Powder Diffraction Standards (JCPDS) card number 29-1129). These peaks are slightly widened in comparison with the XRD peaks of a perfectly-crystalline SiC; the size of ordered (crystallite) domains calculated by a simple Scherrer model from the XRD peak width corresponds to 20 nm. A small shoulder of the (111) peak observed at $34.35^\circ 2\theta$ may indicate the presence of either hexagonal polytype SiC admixtures or the stacking faults within the 3C-SiC structure⁶⁵.

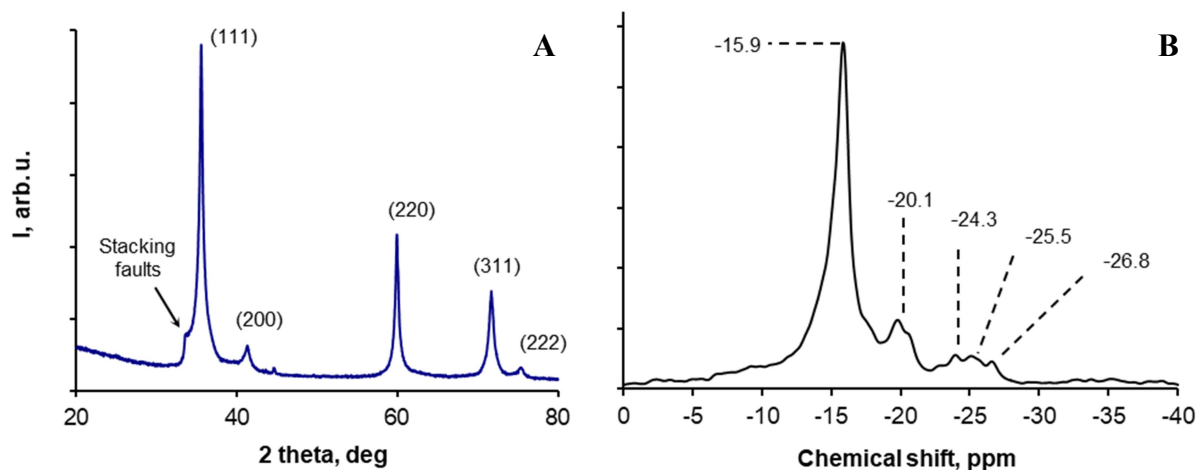


Fig. 4. A) Powder XRD pattern of por-SiC sample; B) ^{29}Si MAS NMR of por-SiC.

Additional structural information of the por-SiC was exhibited by ^{29}Si MAS-NMR studies (Fig. 4B). According to the literature data⁶⁶⁻⁶⁸, the signal at -16 ppm corresponds to cubic “type-A” coordination of Si atoms, while the signals at -20 and -25 ppm belong respectively to “type-C” and “type-B” hexagonal arrangements of Si, appearing in 6H-SiC and 15R-SiC polytypes. No other signals (such as ones from the SiO_2 and SiOC observed in the polymer-derived por-SiC in ref.²⁹) were found. Narrow profiles of the MAS-NMR signals confirm high structural ordering of the SiC crystals. Splitting of the signals at -20 and at -25 ppm into narrow components cannot be related to any of the commonly existing hexagonal SiC polytypes. Hence, these signals relate most probably to Si atoms in hexagonal structural layers disordered within the main 3C-SiC structure (i.e. in the stacking faults or their clusters).

The transmittance FTIR spectrum (Fig. 5A) of por-SiC demonstrates an intense narrow band at 805 cm^{-1} (TO SiC phonon) and a small band at 964 cm^{-1} (LO SiC phonon). No other

bands could be assigned in these spectral conditions due to their low intensity. The por-SiC sample demonstrates good stability towards thermal oxidation (1 h in air at 500°C): no changes in the transmittance FTIR spectrum except appearance of a small band of the surface oxide ($\nu(\text{Si-O})$, 1070 cm^{-1}) was observed for the thermally oxidized sample; morphological parameters derived from the N_2 -isotherm remained unchanged within the accuracy of the method.

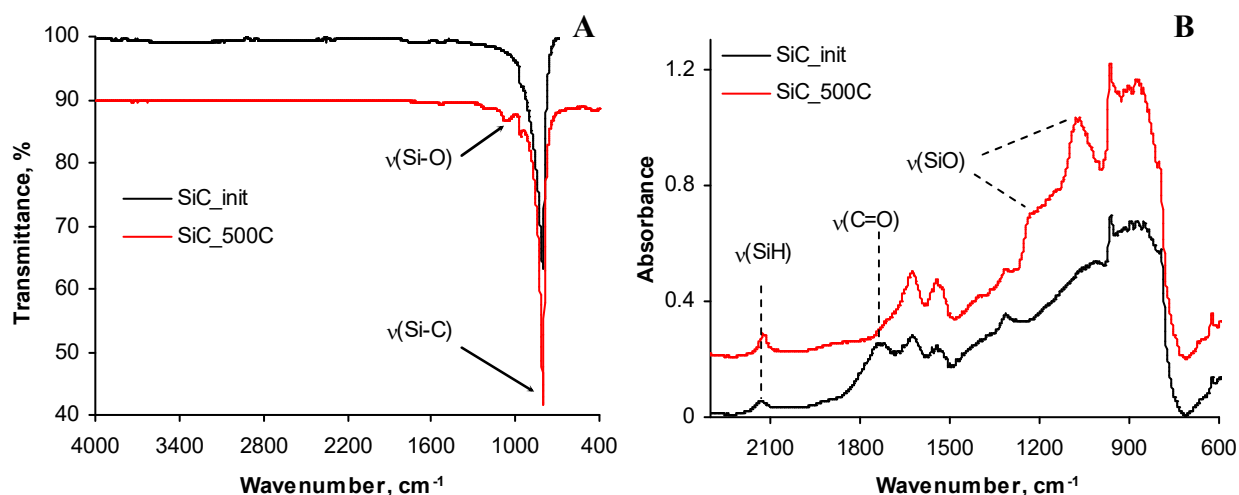


Fig. 5. FTIR spectra of initial and thermally oxidized (500 °C, 1 h in air) por-SiC samples. A) Transmittance, KBr pellets; B) Diffuse reflectance, neat samples.

Note, that the oxidation at 500 °C resulted in approx. 6% mass lost, while the sample color changed from sand-like to white. The mass loss can be attributed to the burning of carbon-enriched surface sub-layer, similar to one found previously for por-6H-SiC⁶⁰. In fact, this layer as well as a similar layer formed on the SiC NPs after HF/HNO_3 oxidation⁶⁹, could be considered as a layer of chemically bonded CFO. Its presence was confirmed by a band of carboxylic acid surface groups ($\nu(\text{C=O})$, 1740 cm^{-1}) in the diffuse-reflectance FT-IR spectrum (Fig. 5B). This band disappeared in the spectrum of thermally-oxidized por-SiC. Instead, noticeable bands of the surface oxide (1230 and 1080 cm^{-1}) evolved. The band of $\nu(\text{SiH})$ at 2130 cm^{-1} seems unaffected by the oxidation, probably due to restoring of $\equiv\text{Si-H}$ groups through the reaction of strained Si-C bonds on the SiO_2/SiC interface with water vapor of ambient air, as described in Ref.⁶⁹. Other bands observed in the DRIFT spectra relate to vibrations of the SiC lattice (in more details: 900

cm^{-1} – TO SiC distorted by reflectance, so-called “reststrahlen” band⁷⁰, 964 cm^{-1} – LO SiC, 1325 , 1560 and 1640 cm^{-1} – different combination modes).

TEM studies of por-SiC (Fig. 6) revealed a dendritic morphology composed mainly of flat-like $10 - 15\text{ nm}$ thick crystallites and $10 - 50\text{ nm}$ pores. These values are in a good accordance with the N_2 adsorption data described below. The lattice spacing value of the crystallites (0.25 nm) derived from the HR-TEM correlates well with the d_{111} distance of the 3C-SiC (0.252 nm).

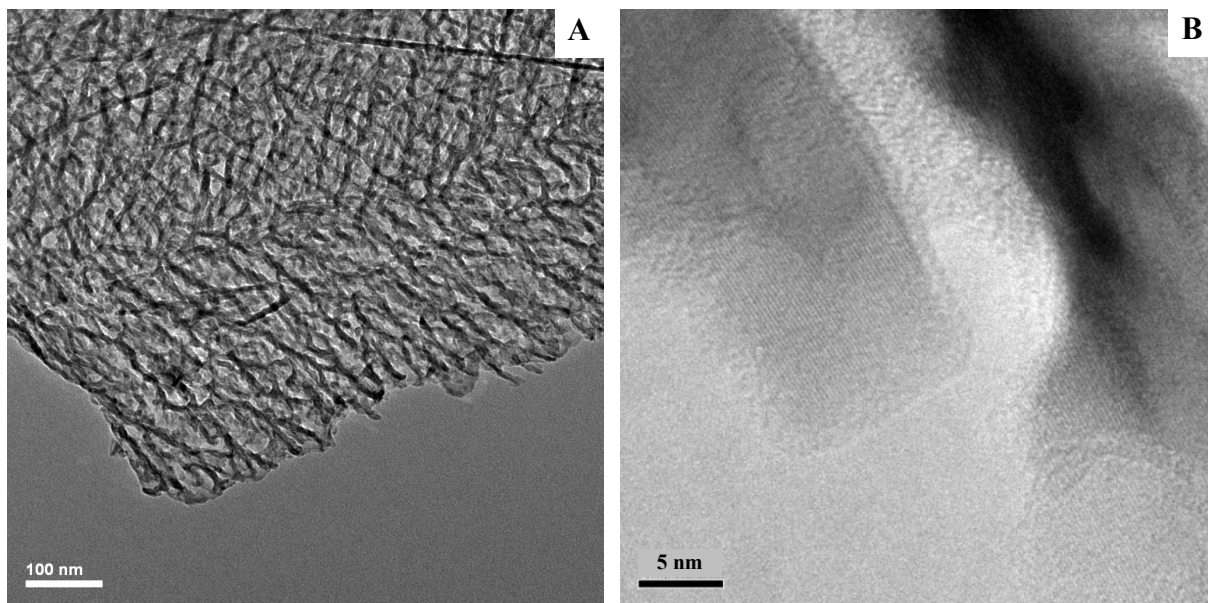


Fig. 6. TEM-images of SiC_{0.7}_HF13_50.

A) Dendritic mesoporous structure; B) Atomic planes and the CFO surface layer.

The chemically bonded CFO surface termination discussed above is clearly observed as 1 nm amorphous layer terminating SiC crystallites. Furthermore, the mass of this layer estimated from its thickness and sample surface area corresponds to 12% of the sample mass. Hence, the 6% mass loss of the sample after the thermal oxidation included the burning of the CFO layer (mass loss) and the silica oxide formation (mass gain).

3.2. Morphology of por-SiC

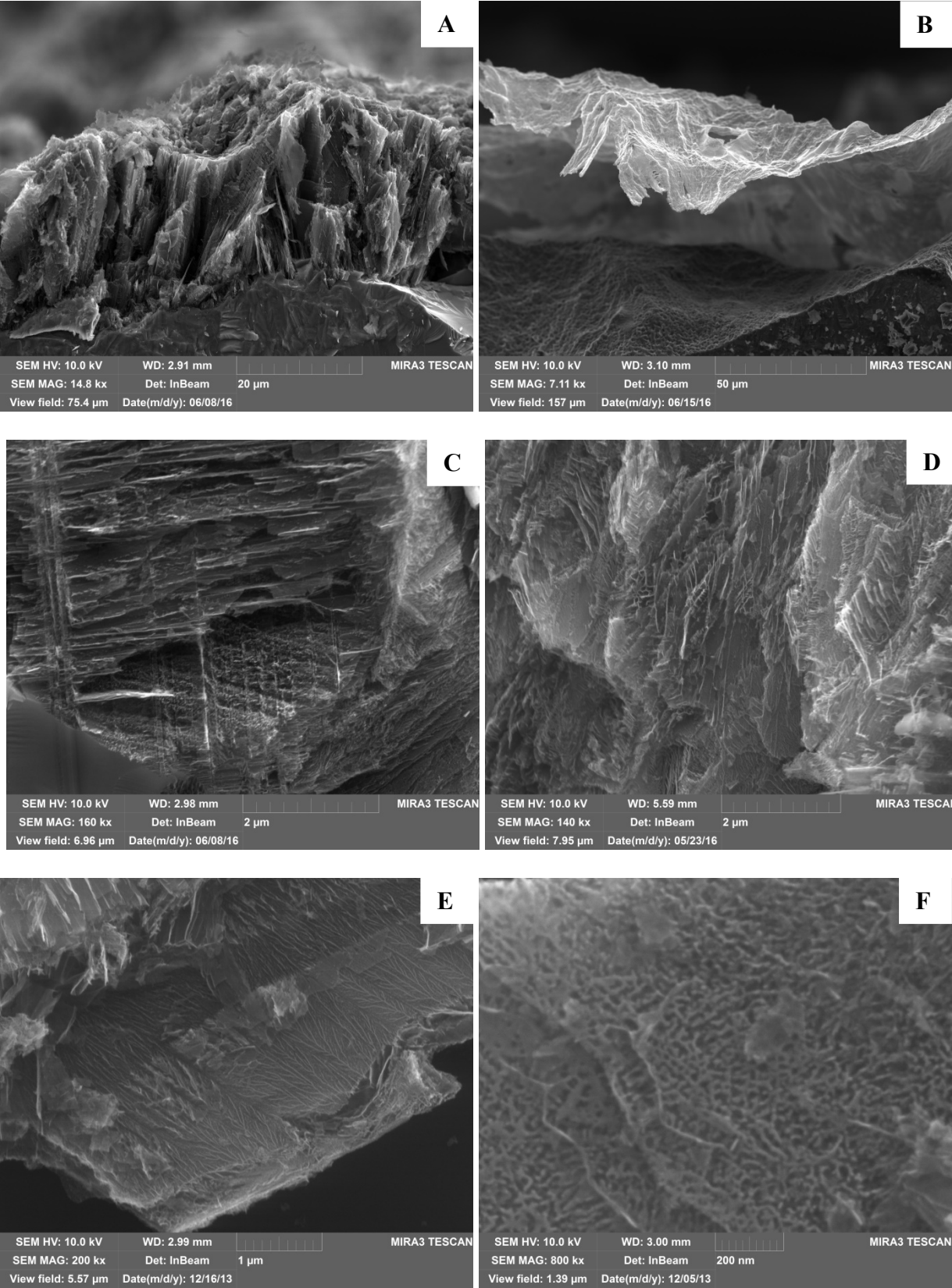
The morphology of porous SiC samples was characterized by scanning electron microscopy (SEM) and N₂ adsorption at 77 K. These methods are complementary to each other: SEM allowed observation of the microstructure, while N₂ adsorption gives averaged surface area, pore volume and size of representative (approx. 100 mg) portion of the sample.

SEM studies of the samples' cross-sections exhibited several tens of micrometers thick porous layers having sharp edges with a SiC bulk (Fig. 7A, S3A). The initial as well as porous SiC surfaces possess approximately 10 μm roughness due to the polycrystalline nature and multiple usages of the plates. The surfaces of SiC plates etched in the “electropolishing” conditions were entirely free of por-SiC (samples sSiC_HF1_50 and sSiC_HF:EtOH(1:1)_50) or were covered by a non-uniform and partially damaged highly-porous layers (samples sSiC_HF13_1000 and sSiC_HF48_50, Fig 7B, S3B). Either electropolishing or mechanical removal of por-SiC layers lead to the surface of bulk SiC with some round pits of about 20-30 nm (Fig. 7B).

Nearly all the samples studied herein exhibit the mixtures of various nanoscale por-SiC morphologies within the layer. However, unlike the numerous publications on the preparation of por-SiC and por-Ge⁴⁰⁻⁵⁸, no morphology dependence on the layer depth was revealed in our studies. Probably, the morphology variations depend mainly on the orientation and electrical conductivity of the SiC crystallites.

Two most typical morphologies coexist in close vicinity for the samples prepared in 2-26% aqueous HF at $j = 25\text{-}200 \text{ mA}\cdot\text{cm}^{-2}$ (Fig. 7C, S3C). The first one, named “hierarchical” could be represented as flat-parallel 50-150 nm spaced layers with mesoporous SiC paddings between them (Fig. 7C-7F, S3C, S3D). The interlayer padding is formed by dendritic (Fig. 7E) and sponge-like SiC crystallite partitions (Fig. 7F) perpendicular to the main layers. The dendrite trunks are located at 100 - 200 nm from each other, the distance between the dendrite branches or small columnar crystallites in sponge-like por-SiC is close to 20 nm. Another type of the

nanostructure, named “tubular” consisted of 100 - 300 nm parallel tubes or slit-like pores, the walls of which are usually oriented perpendicularly or at 35° to the layers of hierarchical structure (Fig. 7C, S3C).



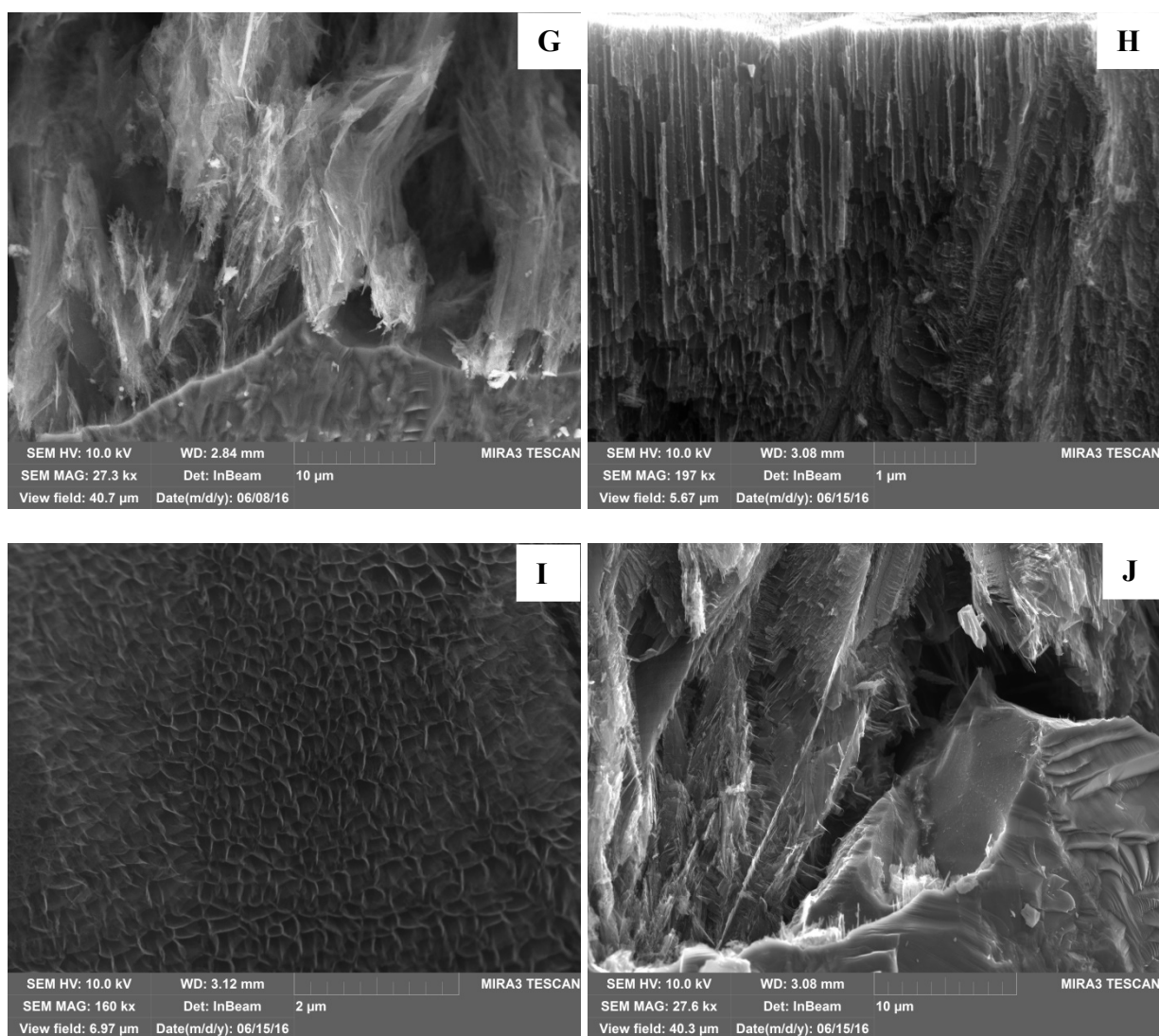


Fig. 7. SEM images of the por-SiC samples.

- A) Rough por-SiC layer on the plate (sSiC_HF26_50);
 B) Pits on the bulk SiC and residual por-SiC after electropolishing (sSiC_HF13_1000);
 C) Coexisting of tubular and hierarchical morphologies (sSiC_HF13_200);
 Hierarchical morphology: D) Overall view (sSiC_HF2_50); E) Top view of dendritic inter-layer filling (SiC_{0.7}_HF13_50); F) Top view of sponge-like inter-layer filling (SiC_{0.7}_HF26_25).
 G) Filamentary morphology (sSiC_HF48_50).
 Tubular morphology: H) Side view (sSiC_HF13_500); I) Tube entrances (sSiC_HF13_1000);
 J) Detachment of porous layer from support (sSiC_HF13_500).

The morphology of por-SiC, prepared in the “electropolish” conditions (Fig. 7G-7J and S4), demonstrates certain deviations in comparison with the one of samples, prepared in diluted aqueous HF at moderate currents. The electropolishing due to the preferable formation of CFO (0.7 mΩ·cm SiC plate, etched in HF:EtOH or 48% HF) resulted in formation of highly-porous SiC having fragile openwork filamentary structure (Fig. 7G). Changes in morphology, caused by the oxide-governed electropolishing (low HF concentrations or high currents) are more

complicated. Particularly, an increase of tubular por-SiC fraction (Fig. 7H, I) accompanied with partial destruction of the hierarchical structure and overall porosity growth (Fig. S4, SI) takes place. Besides that, por-SiC layer partially detaches from the support (Fig. 7J), possibly because of the electrolyte depletion and gas bubbling. Anyway, any por-SiC sample in this work demonstrates the porous texture, represented as complex morphologies mixture.

The morphology of por-SiC flakes, formed in aqueous HF on 1.6 and 4.0 $\text{m}\Omega\cdot\text{cm}$ SiC plates, consisted of hierarchical and tubular porous structures (see Fig. S5), very similar to those found for por-SiC powders, made of 0.7 $\text{m}\Omega\cdot\text{cm}$ plate. However, lower porosity and smaller pore size of the flakes limit their application as catalytic carriers. More likely, the por-SiC fabricated from higher resistivity plates could be applied as nanoreactors or for nanofiltration, similarly to porous silicon free standing layers⁷¹.

Analysis of N_2 isotherms (Fig. 8) confirmed a mesoporous framework for all of the studied por-SiC samples (see the values in table S1, SI). The isotherms relate to type IV with the H3 type hysteresis loop according to the IUPAC classification, typical for mesoporous materials with the slit-like pores⁷². Narrow hysteresis loops and close values of the pore sizes derived from adsorption (pore voids) and desorption (pore entrances) parts of the isotherm (Table S1) indicate an open morphology and the absence of “bottle-like” pores with narrow necks.

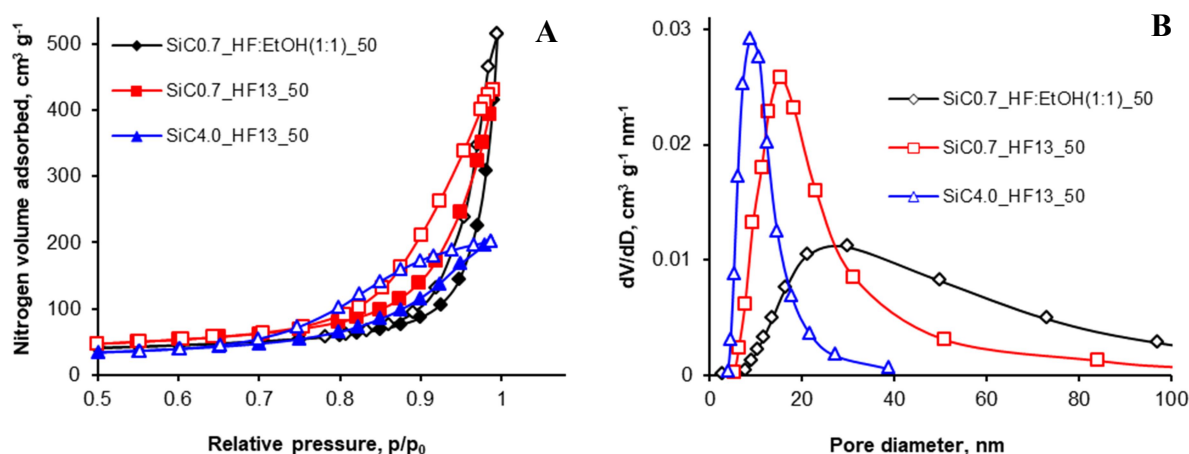


Fig. 8. A) N_2 -adsorption isotherms; B) Pore size distributions (BJH, desorption), typical of por-SiC samples.

The influence of the etching parameters on the morphology of por-SiC is in accordance with the peculiarities exhibited by the material balance. The resistivity of the plate and the electrolyte composition has the most substantial impact on the morphology. Growth of the plate resistivity results in significant decrease in the pore volume and size (Fig. 9) as well as the surface area (Table S1, SI). For the majority of studied samples the value of S_{BET} is in the range of $100 - 120 \text{ m}^2 \text{ g}^{-1}$ and it seems independent on the current density and electrolyte composition.

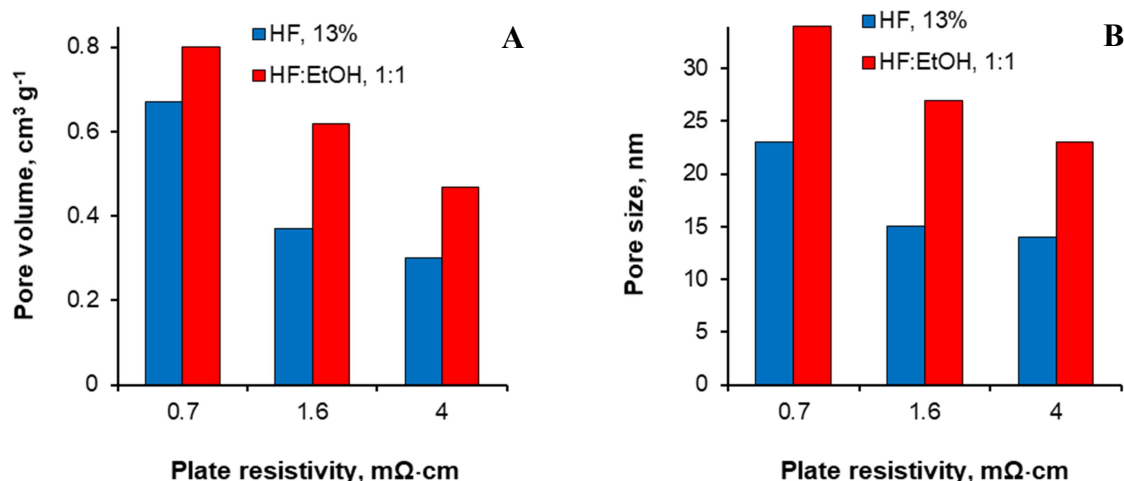


Fig. 9. Dependence of the parameters of por-SiC prepared at $j = 50 \text{ mA}\cdot\text{cm}^{-2}$ (Table 1) on the plate resistivity. A) Pore volume; B) Average pore size (D_{BET}).

Presence of ethanol in the etchant (i.e. CFO-preferable conditions, see Fig. 3 and corresponding discussion) causes the morphology evolution from hierarchical to filamentary one (compare Fig. 7D and 7G). This change is accompanied by a noticeable increase in the pore volume and size (Fig. 9, Table S1). The variations of aqueous HF concentration in 2-26% range show no impact on the morphology type and parameters. Low concentration of HF (1%) causes electropolishing, however minor quantities of por-SiC is formed and detached in the solution during etching and rinsing.

An influence of the current density (j) on the morphological parameters is entirely different for ethanolic and aqueous HF etchants, which is in accordance with the material balance values, discussed above. Growth of j for the HF:EtOH mixture resulted in the shift of

etching conditions from “CFO-preferable” to “por-SiC preferable”. It is accompanied by a significant decrease in the por-SiC pore volume and size (Table S1) and morphology evolution from filamentary to hierarchical. For aqueous HF (13%) growth of j probably gives an increase of tubular pores fraction in “hierarchical-tubular” morphologies mixture. This assumption is confirmed by a partial decrease in the powder yield (Table 1) and surface area (Table S1), SEM images (Fig. 7) and layer thickness growth under constant Q for the samples, prepared at $j = 200 - 500 \text{ mA}\cdot\text{cm}^{-2}$ (Table S2). High j ($1 \text{ A}\cdot\text{cm}^{-2}$) leads to the formation of the non-uniform por-SiC film due to the electropolishing process. The data for the por-SiC prepared in 48% HF appeared irregular because of the spontaneous detachment of porous layers from the plate into the solution during the etching process.

In general, three different, but closely-interconnecting etching modes could be distinguished. The first one, favored by HF (48%) or HF:EtOH etchants and moderate currents, resulted in the preferable formation of the CFO and highly-porous filamentary SiC. The aqueous HF (2-26%) and moderate currents resulted in hierarchical por-SiC, while low HF concentration and high currents resulted in morphology transformation into the tubular one followed by an electropolishing. An increase in the plate resistivity leads to overall decrease of the pore size, porosity and CFO fraction in SiC/CFO mixtures. Voluntary detachment of por-SiC layers from high resistivity plates observed for aqueous HF (13%) probably takes place due to the electrolyte depletion and mechanical action of gas bubbles under the thick por-SiC layers with narrow pores.

Following qualitative physical model could be proposed to interpret the observed experimental trends. Similarly to the classical process of por-Si formation⁶⁴, the anodization of SiC could be described by two stages: electrochemical oxidation of SiC and silicon oxide dissolution in HF. High currents (or low HF concentrations) resulted in the higher rate of oxidation (which is directly specified by the j value) as compared to oxide removal. In this case, the reaction takes place by the electrons tunneling through the surface oxide layer occurring in

the places of highest electric field gradient, i.e. at the pore tips. This leads to the formation of tubular morphology and electropolishing as an extreme case. Probably, these conditions do not facilitate formation of the CFO, and the dissolution of SiC occurs via the reactions 2 and 3.

An increase in the HF concentration (or decrease in the current) changes the situation to the opposite: the SiC surface can be considered as entirely free of oxide during the etching course. In this case, the CFO is formed as the main product of SiC oxidation. Let's remind, that the dissolution of highly-doped n-type SiC in the dark at low voltages ($U \leq 12V$ between two electrodes of the overall cell) proceeds via the holes tunneling through the "space charge region" (SCR). The width of the SCR (d_{SCR}) is proportional to $p^{-1/2}$ (where p is the charge carriers concentration)⁷³, while the probability of tunneling is proportional to $\exp(-d_{SCR})$. As a result, the etching proceeding by this mechanism is predominantly governed by the concentration of holes in the near-surface region. The concentrations of holes in the volume of the studied $0.7-4 \text{ m}\Omega \cdot \text{cm}$ SiC plates are sufficiently high. However, the etched interface could be depleted in the holes due to next factors: i) Quantum confinement in small SiC crystallites, and ii) Charge carriers trapping onto the surface defects. The factor of quantum confinement is responsible for the pore volume decrease and the SiC yields growth with the increase in plate resistivity. For low initial concentration of holes (the case of $4 \text{ m}\Omega \cdot \text{cm}$ plate) relatively large crystallites are sufficient to stop the dissolution, leading to por-SiC with thick pore walls and low pore volume, while for $0.7 \text{ m}\Omega \cdot \text{cm}$ plates the pore walls of por-SiC are much thinner. The factor of charge carriers trapping is responsible for morphology change with growth of the HF concentration or with the addition of EtOH. Both of these factors facilitate the formation of CFO and probably are efficient in surface defects passivation. The passivation, similarly as it occurs for p^+ -type por-Si under the action of HF ⁷⁴, resulted in the release of charge carriers trapped onto the surface defects. Increase in the carriers' concentration resulted in overall thinning of the SCR and highly porous filamentary por-SiC with small crystallites formation.

4. Conclusions

It is the first detailed study of the electrochemical dissolution of highly-doped n-type ($\sim 1 \text{ m}\Omega\cdot\text{cm}$) polycrystalline 3C-SiC plates in aqueous and ethanolic HF. Perfectly crystalline por-SiC with large pore volume, close to $100 \text{ m}^2/\text{g}$ surface area and mesoporous open morphology along with the “carbon fluoro-oxide” byproduct were prepared in gram quantities. The surface of por-SiC is covered with a thin carbon-enriched layer bearing carboxylic acid groups. This type of por-SiC can be used as a catalytic carrier in the Fischer-Tropsch process demonstrating high thermal conductivity, chemical inertness, and mechanical stability. The potential application also includes nanofiltration, nanoreactors and sensors technology.

The parameters, allowing to control of the por-SiC yield, morphology and the SiC/CFO ratio in the product were found and interpreted in terms of quantum confinement and surface passivation. Particularly, the porosity and yield of the por-SiC are governed mainly by the plate resistivity, since the growth of the pore wall thickness while resistivity increases. Three types of the por-SiC morphology, intimately mixed in different ratios within the sample, were usually observed. Highly-porous filamentary por-SiC is formed at low currents in 48% HF or HF:EtOH (1:1) as a mixture with CFO. The etching at moderate currents in aqueous HF mainly provides “hierarchical” por-SiC formed by flat-parallel 50-150 nm spaced layers with mesoporous SiC paddings between them. Higher currents turn the morphology to macroporous “tubular” one consisted of 100 - 300 nm parallel tubes and slit-like pores. High currents and low HF concentrations, as well as the etching in the “CFO-preferable” conditions, resulted in the electropolishing of SiC plate surface: no porous layer resided after the rinsing.

All the results, obtained in the frames of our work, give new understanding of the processes of top-fabrication of SiC nanostructures. The found insights can be also useful for elaboration of por-SiC by chemical and metal-assisted approaches. Finally, our results will allow enlarging of the practical applications field of the por-SiC.

Supporting Information

The Supporting Information is available free of charge on the ACS Publications website.

There are: SEM images and optical photos of the samples, optical photos of the electrochemical cell and CFO solution, tables with morphological parameters (S_{BET} , V_{s} , D_{por}) and por-SiC layer thicknesses.

Acknowledgments

The authors are grateful to Dr. Sergei Khainakov (University of Oviedo, Spain) for MAS NMR characterizations. This work was supported by EU FP-7 MSCA-IRSES grant (GA #319013, “Porous Silicon Carbide as a Support for Co Metal Nanoparticles in Fischer-Tropsch Synthesis”) and EU Horizon 2020 MSCA-RISE grant (Project 690945 “Carbon-based nano-materials for theranostic application”) which are gratefully acknowledged.

References

1. Shackelford, J. F.; Alexander, W., Eds.; *Materials Science and Engineering Handbook*, 3rd ed.; CRC Press LLC: **2001**.
2. Leroi, P.; Madani, B.; Pham-Huu, C.; Ledoux, M.-J.; Savin-Poncet, S.; Bousquet, J. L. Ni/SiC: A Stable and Active Catalyst for Catalytic Partial Oxidation of Methane. *Catal. Today* **2004**, *91-92*, 53-58.
3. Liu, Y.; Ersen O.; Meny, C.; Luck, F.; Pham-Huu, C. Fischer-Tropsch Reaction on a Thermally Conductive and Reusable Silicon Carbide Support. *ChemSusChem*. **2014**, *7*, 1218–1239.
4. Díaz, J. A.; Calvo-Serrano, M.; de la Osa, A. R.; García-Minguillán, A. M.; Romero, A.; Giroir-Fendler, A.; Valverde, J. L. β -silicon Carbide as a Catalyst Support in the Fischer–Tropsch Synthesis: Influence of the Modification of the Support by a Pore Agent and Acidic Treatment. *Appl. Catal. A* **2014**, *475*, 82–89.
5. Labuschagne, J.; Meyer, R.; Chonco, Z. H.; Botha, J. M.; Moodley, D. J. Application of Water-Tolerant Co/ β -SiC Catalysts in Slurry Phase Fischer–Tropsch Synthesis. *Catal. Today* **2016**, *275*, 2-10.
6. Liu, H.; She, G.; Mu, L.; Shi, W. Porous SiC Nanowire Arrays as Stable Photocatalyst for Water Splitting under UV Irradiation. *Mater. Res. Bull.* **2012**, *47*, 917–920.
7. Wang, B.; Wang, Y.; Lei, Y.; Wu, N.; Gou, Y.; Han, C.; Xie, S.; Fang, D. Mesoporous Silicon Carbide Nanofibers with in Situ Embedded Carbon for Co-catalyst Free Photocatalytic Hydrogen Production. *Nano Res.* **2016**, *9*, 886-898.
8. Jiao, Z.; Zhai, Z.; Guo, X.; Guo, X.-Y. Visible-Light-Driven Photocatalytic Suzuki-Miyaura Coupling Reaction on Mott-Schottky-type Pd/SiC Catalyst. *J. Phys. Chem. C* **2015**, *119*, 3238–3243.
9. Oliveros, A.; Guiseppi-Elie, A.; Sadow, S. E. Silicon Carbide: A Versatile Material for Biosensor Applications. *Biomed. Microdevices* **2013**, *15*, 353–368.
10. Alper, J. P.; Kim, M. S.; Vincent, M.; Hsia, B.; Radmilovic, V.; Carraro, C.; Maboudian, R. Silicon Carbide Nanowires as Highly Robust Electrodes for Micro-supercapacitors. *J. Power Sources*, **2013**, *230*, 298–302.
11. Kim, M.; Oh, I.; Kim, J. Hierarchical Porous Silicon Carbide with Controlled Micropores and Mesopores for Electric Double Layer Capacitors. *J. Power Sources* **2015**, *282*, 277–285.
12. Yan, P.; Xu, J.; Wu, Ch.; Gu, Yu; Zhang, X.; Zhang, R.; Song, Y. High-power Supercapacitors Based on Hierarchical Porous Nanometer-sized Silicon Carbide-derived Carbon. *Electrochim. Acta* **2016**, *189*, 16–21.
13. Deng, W.; Yu, X.; Sahimi, M.; Tsotsis, T. T. Highly Permeable Porous Silicon Carbide Support Tubes for the Preparation of Nanoporous Inorganic Membranes. *J. Membr. Sci.* **2014**, *451*, 192–204.
14. Zhu, J.; Liu, Z.; Wu, X. L.; Xu, L. L.; Zhang, W. C.; Chu., P. K. Luminescent Small-diameter 3C-SiC Nanocrystals Fabricated via a Simple Chemical Etching Method. *Nanotechnology* **2007**, *18*, 365603.
15. J Botsoa, J.; Lysenko, V.; Géloën, A.; Marty, O.; Bluet, J.-M.; Guillot, G. Application of 3C-SiC quantum Dots for Living Cell Imaging. *Appl. Phys. Lett.* **2008**, *92*, 173902.
16. Beke, D.; Szekrenyes, Z.; Balogh, I.; Czigany, Z.; Kamaras, K.; Gali, A. Preparation of Small Silicon Carbide Quantum Dots by Wet Chemical Etching. *J. Mater. Res.*, **2013**, *28*, 44-49.
17. Mwania, M.; Janáky, C.; Rajeshwar, K.; Kroll, P. Fabrication of β -SiC Quantum Dots by Photo-assisted Electrochemical Corrosion of Bulk Powders. *Electrochem. Commun.* **2013**, *37*, 1-4.
18. Shcherban, N. D. Review on Synthesis, Structure, Physical and Chemical Properties and Functional Characteristics of Porous Silicon Carbide. *J. Ind. Eng. Chem.* **2017**, *50*, 15–28.
19. Yang, Zh.; Xia, Y.; Mokaya, R. High Surface Area Silicon Carbide Whiskers and Nanotubes Nanocast using Mesoporous Silica. *Chem. Mater.* **2004**, *16*, 3877–3884.

20. Gorzkowski, E. P.; Qadri, S. B.; Rath, B. B.; Goswami, R.; Caldwell, J. D. Formation of Nanodimensional 3C-SiC Structures from Rice Husks. *J. Electron. Mater.* **2013**, *42*, 799–804.
21. Dasog, M.; Smith, L. F.; Purkait, T. K.; Veinot, J. G. C. Low Temperature Synthesis of Silicon Carbide Nanomaterials using a Solid-state Method. *Chem. Commun.* **2013**, *49*, 7004–7006.
22. Mojarad, B. S.; Nourbakhsh, A.; Kahrizsangi, R. E.; Masoud, M.; MacKenzie, K. J. D. Synthesis of Nanostructured SiC by Magnesiothermal Reduction of Silica from Zeolite ZSM-5 and Carbon: The Effect of Carbons from Different Sources. *Ceram. Int.* **2015**, *41*, 5287–5293.
23. Ledoux, M. J.; Hantzer, S.; Pham Huu, C.; Guille, J.; Desaneaux, M.-P. New Synthesis and Uses of High-specific-surface SiC as a Catalytic Support that is Chemically Inert and Has High Thermal Resistance. *J. Catal.* **1988**, *114*, 176–185.
24. Nguyen, P.; Pham, C. Innovative Porous SiC-based Materials: From Nanoscopic Understandings to Tunable Carriers Serving Catalytic Needs. *Appl. Catal. A* **2011**, *391*, 443–454.
25. Liu, Zh.; Shen, W.; Bu, W.; Chen, H.; Hua, Z.; Zhang, L.; Li, L.; Shi, J.; Tan, Sh. Low-temperature Formation of Nanocrystalline β -SiC with High Surface Area and Mesoporosity via Reaction of Mesoporous Carbon and Silicon Powder. *Microporous Mesoporous Mater.* **2005**, *82*, 137–145.
26. Yukhymchuk, V. O.; Kiselov, V. S.; Valakh, M. Ya.; Tryus, M. P.; Skoryk, M. A.; Rozhin, A. G.; Kulinich, S. A.; Belyaev, A. E.; Biomorphous SiC Ceramics Prepared from Cork Oak as Precursor. *J. Phys. Chem. Solids* **2016**, *91*, 145–151.
27. Shi, Y.; Meng, Y.; Chen, D.; Cheng, S.; Chen, P.; Yang, H.; Wan, Y.; Zhao, D. Highly Ordered Mesoporous Silicon Carbide Ceramics with Large Surface Areas and High Stability. *Adv. Funct. Mater.* **2006**, *16*, 561–567.
28. Krawiec, P.; Schrage, C.; Kockrick, E.; Kaskel, S. Tubular and Rodlike Ordered Mesoporous Silicon (Oxy)carbide Ceramics and their Structural Transformations. *Chem. Mater.* **2008**, *20*, 5421–5433.
29. Hoffmann, C.; Biemelt, T.; Seifert, A.; Pinkert, K.; Gemming, T.; Spange, S.; Kaskel, S. Polymer-derived Nanoporous Silicon Carbide with Monodisperse Spherical Pores. *J. Mater. Chem.* **2012**, *22*, 24841–24847.
30. Alekseev, S. A.; Korytko, D. M.; Gryn, S. V.; Iablokov, V.; Khainakova, O. A.; Garcia-Granda, S.; Kruse, N. Silicon Carbide with Uniformly Sized Spherical Mesopores from Butoxylated Silica Nanoparticles Template. *J. Phys. Chem. C* **2014**, *118*, 23745–23750.
31. Nardin, T.; Cambedouzou, J.; Ravoux, J.; Rey, C.; Meyer, D.; Diat, O. Elaborating ordered silicon carbide nanorods by preceramic polymer nanocasting, *RSC Adv.*, **2015**, *5*, 86156–86162.
32. Nardin, T.; Gouze, B.; Cambedouzou, J.; Bauduin, P.; Wong Chi Man, M.; Deschanel, X.; Bourgeois, D.; Meyer, D.; Diat, O. Elaboration of Porous Silicon Carbide by Soft Templating Molecular Precursors with Semifluorinated Alkanes, *J. Mater. Chem. A* **2015**, *3*, 3082–3090.
33. Nghiem, Q. D.; Kim, D.-P. Direct Preparation of High Surface Area Mesoporous SiC-Based Ceramic by Pyrolysis of a Self-Assembled Polycarbosilane-*block*-Polystyrene Diblock Copolymer, *Chem. Mater.* **2008**, *20*, 3735–3739.
34. Nardin, T.; Gouze, B.; Cambedouzou, J.; Diat, O. Soft Templated Mesoporous SiC from Polycarbosilane Grafted onto Triblock Copolymers. *Mater. Lett.* **2016**, *185*, 424–427.
35. Wang, K.; Yao, J. F.; Wang, H. T.; Cheng, Y. B. Effect of Seeding on Formation of Silicon Carbide Nanostructures from Mesoporous Silica-Carbon Nanocomposites. *Nanotechnology* **2008**, *19*, 175605.
36. Hasselman, D. P. H. Role of Structure and Composition in the Heat Conduction Behavior of Silicon Carbide. In Hasselman, D. P. H. and Thomas Jr., J. R., Eds.; *Thermal Conductivity 20*, Plenum Press: **1989**, pp. 141–153.
37. Wijesundara, M. B. J.; Azevedo, R. G. *Silicon Carbide Microsystems for Harsh Environments*; Springer-Verlag: **2011**.

38. Zhuang, D.; Edgar, J. H. Wet Etching of GaN, AlN and SiC: A Review. *Mat. Sci. Eng. R* **2005**, *48*, 1–46.
39. Canham, L. T. Silicon Quantum Wire Array Fabrication by Electrochemical and Chemical Dissolution of Wafers. *Appl. Phys. Lett.* **1990**, *57*, 1046–1048.
40. Shor, J. S.; Zhang, X. G.; Osgood, R. M. Laser-assisted Electrochemical Etching of n-type beta-SiC. *J. Electrochem. Soc.* **1992**, *139*, 1213–1216.
41. Shor, J. S.; Bemis, L.; Kuttz, A. D.; Grimberg, I.; Weiss, B. Z.; MacMillian, M. F.; Choyke, W. J. Characterization of Nanocrystallites in Porous p-type 6H-SiC. *J. Appl. Phys.* **1994**, *76*, 4045–4049.
42. Matsumoto, T.; Takahashi, J.; Tamaki, T.; Futagi, T.; Mimura, H.; Kanemitsu, Y. Blue-green Luminescence from Porous Silicon Carbide. *Appl. Phys. Lett.* **1994**, *64*, 226–228.
43. Konstantinov, A. O.; Henry, A.; Harris, C. J.; Jansen, E. Photoluminescence Studies of Porous Silicon Carbide. *Appl. Phys. Lett.* **1995**, *66*, 2250–2252.
44. Choyke, W. J.; Matsunami, H.; Pensl, G. *Silicon Carbide: Recent Major Advances*. Springer Science & Business Media: **2003**.
45. Shor, J.S.; Grimberg, I.; Weiss, B.Z.; Kurtz, A.D. Direct Observation of Porous SiC Formed by Anodization in HF. *Appl. Phys. Lett.* **1993**, *62*, 2836–2838.
46. Shishkin, Y.; Choyke, W. J.; Devaty, R. P. Photoelectrochemical Etching of n-type 4H Silicon Carbide. *J. Appl. Phys.* **2004**, *96*, 2311–2322.
47. Shishkin, Y.; Ke, Y.; Devaty, R. P.; Choyke, W. J. A Short Synopsis of the Current Status of Porous SiC and GaN. *Mater. Sci. Forum* **2004**, *483–485*, 251–256.
48. Newby, P.; Bluet, J.-M.; Aimez, V.; Fréchette, L. G.; Lysenko, V. Structural Properties of Porous 6H Silicon Carbide. *Phys. Status Solidi. C* **2010**, *8*, 1950–1953.
49. Zangoie, S.; Arwin, H. Surface, Pore Morphology, and Optical Properties of Porous 4H-SiC. *J. Electrochem. Soc.* **2001**, *148*, G297–G302.
50. Gautier, G.; Cayrel, F.; Capelle, M.; Billoué, J.; Song, X.; Michaud, J.-F.; Room Light Anodic Etching of Highly Doped n-type 4H-SiC in High-concentration HF Electrolytes: Difference Between C and Si Crystalline Faces. *Nanoscale Res. Lett.* **2012**, *7*, 367.
51. Gautier, G.; Biscarrat, J.; Valente, D.; Defforge, T.; Gary, A.; Cayrel, F. Systematic Study of Anodic Etching of Highly Doped n-type 4H-SiC in Various HF Based Electrolytes. *J. Electrochem. Soc.* **2013**, *160*, D372–D379.
52. Shishkin, Y.; Ke, Y.; Devaty, R. P.; Choyke, W. J. Fabrication and Morphology of Porous p-type SiC. *J. Appl. Phys.* **2005**, *97*, 044908.
53. Soloviev, S.; Das, T.; Sudarshan, T. S. Structural and Electrical Characterization of Porous Silicon Carbide Formed in n-6H-SiC Substrates. *Electrochem. Solid-State Lett.* **2003**, *6*, G22–G24.
54. Rittenhouse, T.L.; Bohna, P.W.; Hossain, T. K.; Adesida, I.; Lindesay, J.; Marcus, A. Surface-state Origin for the Blueshifted Emission in Anodically Etched Porous Silicon Carbide. *J. Appl. Phys.* **2004**, *95*, 490–496.
55. Sagar, A.; Lee, C. D.; Feenstra, R. M.; Inoki, C. K.; Kuan, T. S. Morphology and Effects of Hydrogen Etching of Porous SiC. *J. Appl. Phys.* **2002**, *92*, 4070–4074.
56. Tutashkonko, S.; Alekseev, S.; Nychporuk, T. Nanoscale Morphology Tuning of Mesoporous Ge: Electrochemical Mechanisms. *Electrochim. Acta* **2015**, *180*, 545–554.
57. Wang, L.; Shao, H.; Hu, X.; Xu, X. Hierarchical Porous Patterns of n-type 6H-SiC Crystals via Photoelectrochemical Etching. *J. Mater. Sci. Technol.* **2013**, *29*, 655–661.
58. Shor, J. S.; Kurtz, A. D. Photoelectrochemical Etching of 6H-SiC. *J. Electrochem. Soc.* **1994**, *141*, 778–781.
59. Alekseev, S.; Korytko, D.; Iazykov, M.; Khainakov, S.; and Lysenko, V. Electrochemical Synthesis of Carbon Fluorooxide Nanoparticles from 3C-SiC Substrates. *J. Phys. Chem. C* **2015**, *119*, 20503–20514.

60. Alekseev, S. A.; Zaitsev, V. N.; Botsoa, J.; Barbier, D. Fourier Transform Infrared Spectroscopy and Temperature-Programmed Desorption Mass Spectrometry Study of Surface Chemistry of Porous 6H-SiC. *Chem. Mater.* **2007**, *19*, 2189-2194.
61. Senthilnathan, J.; Weng, Ch.-Ch.; Tsai, W.-T. Synthesis of Carbon Films by Electrochemical Etching of SiC with Hydrofluoric Acid in Nonaqueous Solvents. *Carbon* **2014**, *71*, 181–189.
62. Iablokov, V.; Gryn, S. V.; Alekseev, S. A.; Kruse, N. Fabrication of Supported Size-controlled Cobalt Nanoparticles over Porous Silicon Carbide for Superior Catalytic Performance in the Fischer-Tropsch Process. 734f, AIChE Annual Meeting **2017**, Minneapolis, USA.
63. CVD Silicon Carbide Technical Data Sheet.
https://www.dow.com/assets/attachments/business/gt/advanced_ceramics/cvd_silicon_carbide/tds/cvd_silicon_carbide.pdf (accessed Apr 26, 2018).
64. Lehmann, V., Ed.; *Electrochemistry of Silicon: Instrumentation, Science, Materials and Applications*. Wiley: **2002**.
65. Pujar, V.V.; Cawley, J.D. Effect of Stacking Faults on the X-ray Diffraction Profiles of β -SiC Powders. *J. Am. Ceram. Soc.* **1995**, *78*, 774–782.
66. Guth, J. R.; Petuskey, W. T. Silicon-29 Magic-angle-spinning NMR Characterization of Silicon Carbide Polytypes. *J. Phys. Chem.* **1987**, *91*, 5361–5364.
67. Hartman, J. S.; Richardson, M. F.; Sherriff, B. L.; Winsborrow, B. G. Magic Angle Spinning NMR Studies of Silicon Carbide: Polytypes, Impurities, and Highly Inefficient Spin-lattice Relaxation. *J. Am. Chem. Soc.* **1987**, *109*, 6059–6067.
68. Richardson, M. F.; Hartman, J. S.; Guo, D.; Winsborrow, B. G. NMR Chemical Shift Tensors and Peak Assignments for the 6H Polytype of Silicon Carbide. *Chem. Mater.* **1992**, *4*, 318–323.
69. Alekseev, S.; Shamatulskaya, E.; Volvach, M.; Gryn, S.; Korytko, D.; Bezverkhyy, I.; Iablokov, V.; Lysenko, V. Size and Surface Chemistry Tuning of Silicon Carbide Nanoparticles. *Langmuir* **2017**, *33*, 13561–13571.
70. MacMillan, M.F.; Devaty, R. P.; Choyke, W. J.; Goldstein, D. R.; Spanier, J. E.; Kurtz, A. D. Infrared Reflectance of Thick p-type Porous SiC layers. *J. Appl. Phys.* **1996**, *80*, 2412–2419.
71. Serdiuk, T.; Lysenko, V.; Alekseev, S.; Skryshevsky, V. A. Size Tuning of Luminescent Silicon Nanoparticles with Meso-porous Silicon Membranes. *J. Colloid Interface Sci.* **2011**, *364*, 65–70.
72. Gregg, S., Sing, K. S. W. *Adsorption, surface area and porosity*, 2nd ed.; Willey: **1982**.
73. Memming, R. *Semiconductor Electrochemistry*, Willey-VCH: **2011**.
74. Oliinyk, B. V.; Lysenko, V.; Alekseev, S. Determining the Impact of Hydrofluoric Acid on Surface States of As-prepared and Chemically Modified Si Nanocrystals. *RSC Adv.*, **2016**, *6*, 3723– 3728.